Available online at www.sciencedirect.com
SCIENCE DIRECT®
International Journal of Heat and Mass Transfer 49 (2006) 3500–3513
International Journal of HEAT and MASS TRANSFER
www.elsevier.com/locate/ijhmt

Numerical simulation of liquid metals in differentially heated enclosure undergoing orthogonal rotation

M.F. Baig *, M. Zunaid

Department of Mechanical Engineering, Aligarh Muslim University, Aligarh 202001, India

Received 6 September 2005
Available online 19 May 2006

Abstract

In this work a numerical investigation has been performed to examine the characteristics of mixed convective heat transfer in square enclosures undergoing orthogonal rotation i.e. rotation axis and gravity axis are orthogonal to each other. A semi implicit finite difference code on a collocated grid is used to solve the momentum and energy equations subject to Boussinesq approximation. The study is carried out for a wide range of operating parameters such as Rayleigh number (Ra), Taylor number (Ta), Rotational Rayleigh number (Ra_w) for a fixed Prandtl number (Pr). The numerical experiments have been carried out for a fixed $Pr = 0.01$, Ra varies from 10^5 to 10^7 while Ta and Ra_w vary from almost 0 to 10^9. Results reveal that significant increase or decrease in heat transfer rates can be achieved by the rotational effects, mainly influenced by centrifugal force.

Keywords: Liquid metals; Coriolis force; Centrifugal force; Orthogonal rotation; Convection; Heat transfer

1. Introduction

The effect of cavity rotation on flow stability as well as heat transfer is particularly very important concerning the flow of liquid metals inside a cavity, which is the standard material for the manufacture of single wafer crystals in the semiconductor industry. Though a vast amount of work, both theoretical and experimental, exists in the open literature related to heat and mass transfer in rotating ducts [1–4] for cases of either air and water, yet little or no work has been done, for low Prandtl number fluids especially in configurations like square ducts undergoing orthogonal rotation.

Some of the results pertaining to either air and water in rotating ducts, channels etc. are summarised herewith. Nguyen et al. [5] have shown that the effect of counter rotating the cavity results in growth of good quality crystals. Mahadevappa et al. [6] found that the heat transfer is more efficient in elliptical geometry ducts, rotating about a parallel axis situated parallel to and away from the central axis, then in rectangular ducts under similar operating conditions. Mixed convection heat and mass transfer have been studied by Lee et al. [7] considering uniform temperature and concentration conditions along the porous duct walls. They concluded that the combined thermal and solutal buoyancies enhance the heat and mass transfer rate along the wetted wall. Theoretical and experimental examination of the effect of Coriolis force on the flow structures for adiabatic rotating channels was performed by Hwang and Jen [8] and it was found that at low rotation rates, a double vortex secondary flow appears in the transverse plan of the channel while at large rotation rates, an instability occurs in the form of longitudinal rolls in the interior of the channel.

Fann and Yang [9] studied the effect of centrifugal buoyancy on the fluid flow and heat transfer characteristics in radially rotating channels for steady laminar flow and they came to the conclusion that the Coriolis force causes the generation or decay of one or multiple pairs of transverse velocities. Turbulent heat convection with fully developed

* Corresponding author. Tel.: +91 9897517071.
E-mail address: drmfbaig@yahoo.co.uk (M.F. Baig).

0017-9310/$ - see front matter © 2006 Elsevier Ltd. All rights reserved.
doi:10.1016/j.ijheatmasstransfer.2006.02.046

Nomenclature

AR	$\frac{L}{H}$ aspect ratio
C_p	specific heat at constant pressure, $\frac{\mathrm{kJ}}{\mathrm{kg\,K}}$
CEF	centrifugal force, $Ra_{\mathrm{w}}Pr\theta\sqrt{X^2+Y^2}$
COR	Coriolis force, $Pr\sqrt{Ta(U^2+V^2)}$
g	magnitude of acceleration due to gravity, $\frac{\mathrm{m}}{\mathrm{s}^2}$
H	depth of fluid layer, m
i, j	indices in the X and Y directions
L	width of fluid layer, m
Nu	space-averaged Nusselt number
p_{m}	motion pressure, $\frac{\mathrm{N}}{\mathrm{m}^2}$
P_{m}	dimensionless motion pressure
Pr	Prandtl number, $\frac{\nu}{\kappa}$
Ra	Rayleigh number, $\frac{\alpha g H^3 \Delta T}{\nu\kappa}$
Ra_{w}	rotational Rayleigh number, $\frac{(\Omega_{\mathrm{d}}^2 H)H^3\alpha\Delta T}{\nu\alpha}$
t	dimensionless time
T	dimensional temperature, K
Ta	Taylor number, $\frac{4\Omega_{\mathrm{d}}^2 H^4}{\nu^2}$
TBF	thermal buoyancy force, $RaPr\theta$
v	(u, v) dimensional velocity field in x and y directions, $\frac{\mathrm{m}}{\mathrm{s}}$
V	(U, V) dimensionless velocity field in X and Y directions
x, y	dimensional coordinate, m
X, Y	dimensionless coordinate

Greek symbols

α	coefficient of thermal expansion, K^{-1}
ΔT	temperature difference between hot and cold walls
τ	dimensional time, s
θ	non-dimensional temperature, $\frac{T-T_{\mathrm{c}}}{\Delta T}$
κ	thermal diffusivity, $\frac{\mathrm{m}^2}{\mathrm{s}}$
ρ	density, $\frac{\mathrm{kg}}{\mathrm{m}^3}$
ρ_0	reference density
ν	kinematic viscosity, $\frac{\mathrm{m}^2}{\mathrm{s}}$
Ω_{d}	dimensional speed of rotation, $\frac{\mathrm{rad}}{\mathrm{s}}$
Ω	non-dimensional rotation speed, $\Omega_{\mathrm{d}}\left(\frac{H^2}{\kappa}\right)$

Subscripts

c	cold wall
h	hot wall
m	motion
0	reference
$\perp$	perpendicular

velocity and temperature fields was studied by Mori et al. [10] in a circular pipe rotating around an axis perpendicular to its own axis. They found that the increase of Nusselt number is not significant for turbulent regions of the flow as compared to laminar regions. Yan [11] numerically studied the characteristics of laminar mixed convection in rectangular ducts rotating about a parallel axis with water film evaporation along the porous ducts walls and concluded that heat and mass transfer is enhanced because of the formation of secondary vortices in the duct.

Song et al. [12], studied the fluid flow and heat transfer model for high speed rotating heat pipe, with substantial centrifugal accelerations. They found that the natural convection in the liquid film becomes more significant at higher accelerations and fluid loadings. Yang and Wang [13] studied the bifurcation structure and stability of combined free and forced convection in a rotating curved duct of square cross-section. Results showed that as the relative strength of buoyancy force decreases, temporal oscillations change from periodic to non-periodic and finally chaotic. Ker and Lin [14] in their study have emphasized that the study of flow behavior for case of liquid metals in rotating cavities needs further investigation. The major difference between flow of liquid metals to comparatively larger Prandtl number fluids such as air, is that the former fluids have higher density and hence are subjected to large centrifugal forces per unit volume as compared to the latter.

The principal motivating factor to study this complex flow of rotating liquids metals is due to the scarcity of literature available pertaining to this configuration, to the

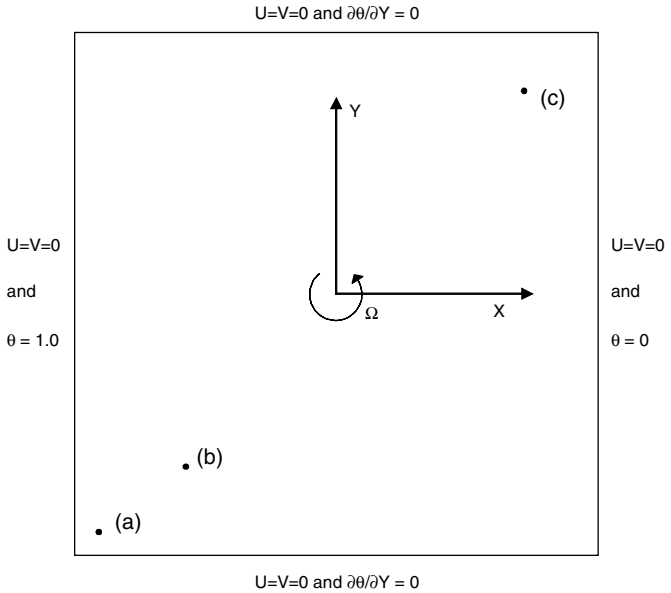

Fig. 1. Schematic diagram of a square enclosure showing boundary conditions and location of spatial points (a), (b) and (c).

best of our knowledge. The present analysis takes into account both the Coriolis and centrifugal forces combined with thermal buoyancy in order to analyse their effects on dynamics of flow and heat transfer.

2. Mathematical formulation

The schematic diagram of the physical system under investigation is depicted in Fig. 1. Initially at time $\tau < 0$, the liquid inside the enclosure is rotating anti-clockwise as a solid body at a constant angular speed Ω, and is isothermal at temperature T_0. At time $\tau \geqslant 0$, the vertical side-walls are suddenly raised and lowered to uniform temperatures $T_h = T_0 + \Delta T/2$ and $T_c = T_0 - \Delta T/2$ while the top and bottom walls are thermally insulated. Thus, the liquid metal inside the cavity is simultaneously subjected to thermal and rotational buoyancy forces. By assuming the Boussinesq approximation in both the gravitational and centrifugal forces, the thermal, centrifugal and Coriolis forces acting on the flow are respectively, equal to $\rho_0 g\alpha(T - T_0)$, $-\rho_0\alpha(T - T_0)\Omega_d \times \Omega_d \times r$ and $-2\rho_0\Omega_d \times V$.

As the gravity, centrifugal and Coriolis forces all lie within the cross-sectional plane of the cavity and on further assuming a long square duct thereby neglecting the end-effects of 3D cavity flow, the problem can be analysed as a two-dimensional flow problem. Thus it is felt that two-dimensional calculations provide a good platform for understanding the basic flow dynamics and the roles played by the time-varying gravitational buoyancy, rotational buoyancy and Coriolis forces in affecting the flow structures. Due to Boussinesq approximation the problem and consequently the results are valid for configurations which

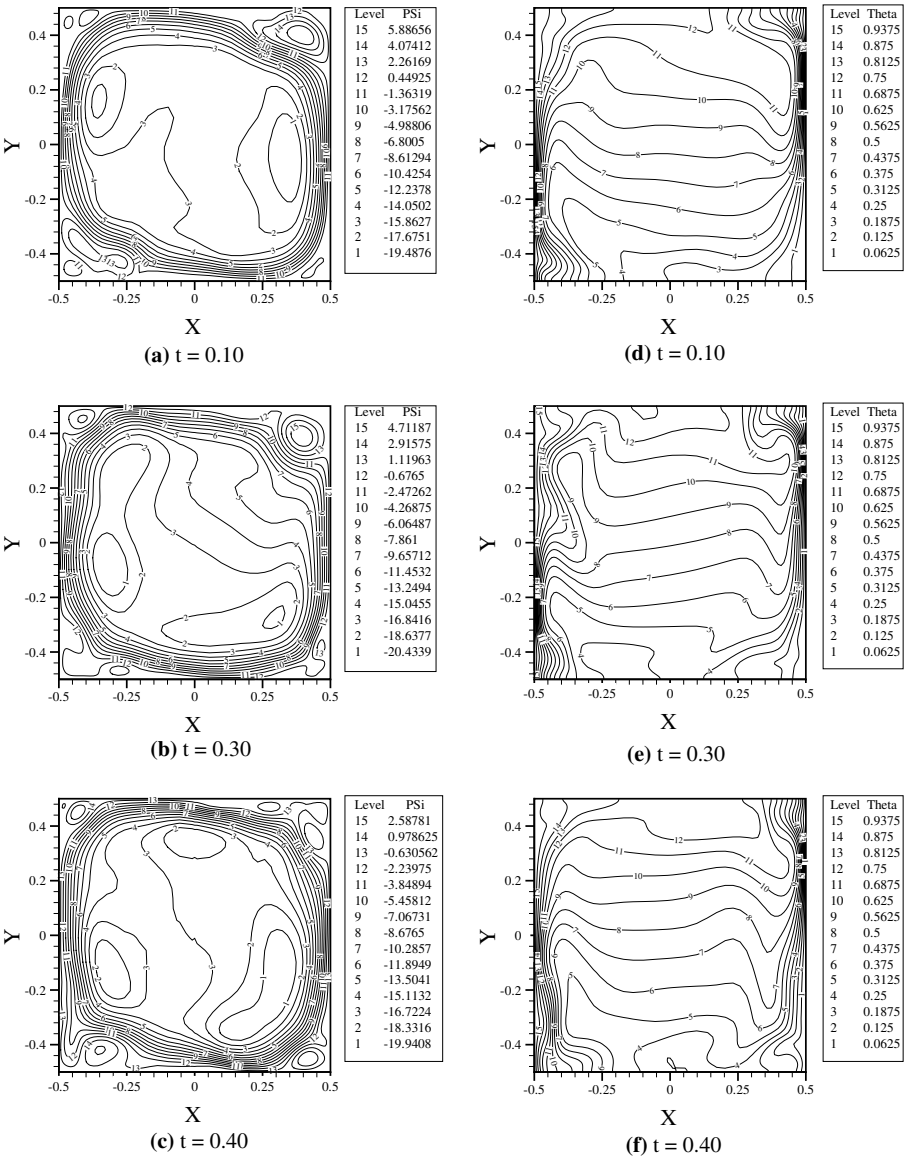

Fig. 2. (a), (b) and (c) show streamline contours while (d), (e) and (f) show isotherm contours at different time instants for $Ra = 10^7$, $Ta = 8.16$ and $Ra_w = 1.02 \times 10^2$.

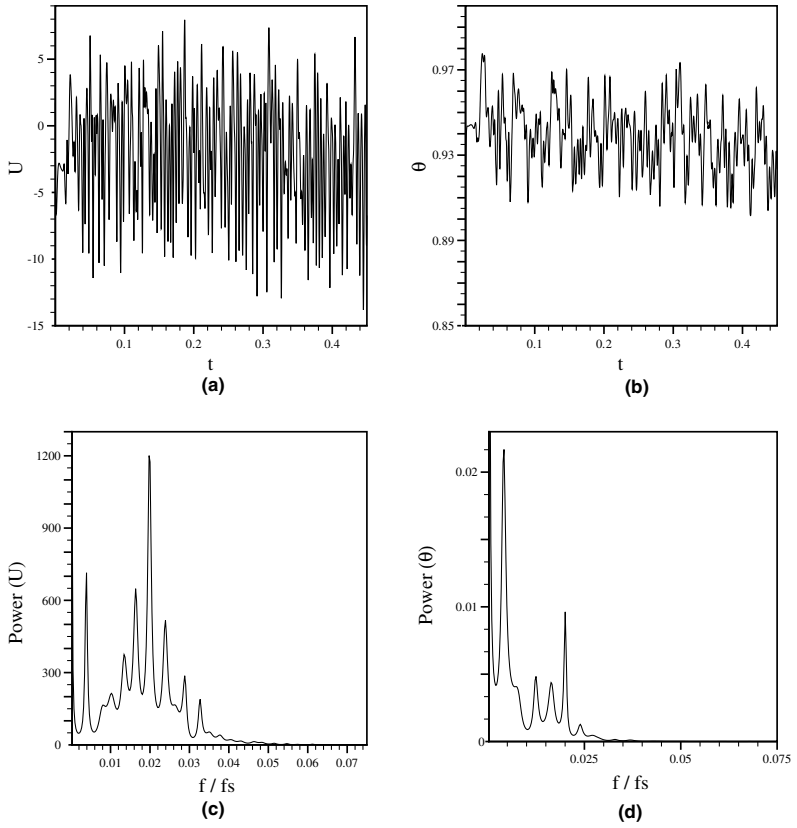

Fig. 3. (a) and (b) show time history while (c) and (d) show power spectrum of horizontal velocity component (U) and temperature (θ) at spatial point (a) for $Ra = 10^7$, $Ta = 8.16$ and $Ra_w = 1.02 \times 10^2$.

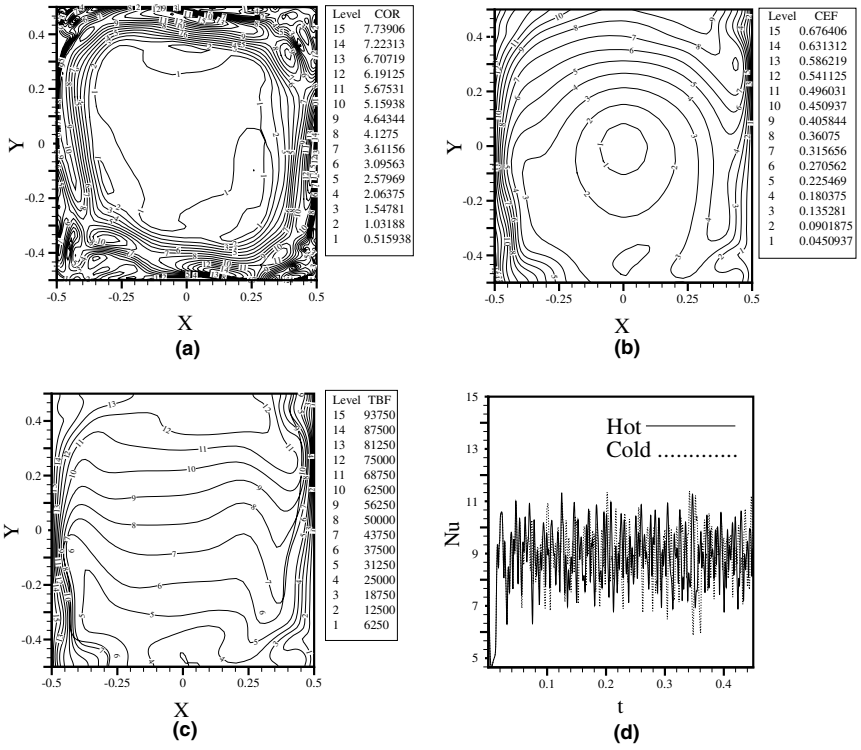

Fig. 4. Depicts spatial variation of (a) Coriolis force, (b) centrifugal force, (c) thermal buoyancy force at $t = 0.4$ and (d) variation of Nusselt number with time for $Ra = 10^7$, $Ta = 8.16$ and $Ra_w = 1.02 \times 10^2$.

have small ΔT and small scale heights compared to the large-scale geophysical systems.

The governing equation of mass, momentum and energy can be expressed in the dimensional form for 2D incompressible flow as follows:

$$\frac{\partial u}{\partial x}+\frac{\partial v}{\partial y}=0 \tag{1}$$

$$\frac{\mathrm{D}u}{\mathrm{D}\tau}=-\frac{1}{\rho_0}\frac{\partial p_\mathrm{m}}{\partial x}+\alpha(T-T_0)g\sin\Omega_\mathrm{d}\tau+\nu\nabla^2 u+2\Omega_\mathrm{d}v-\Omega_\mathrm{d}^2\alpha(T-T_0)x \tag{2}$$

$$\frac{\mathrm{D}v}{\mathrm{D}\tau}=-\frac{1}{\rho_0}\frac{\partial p_\mathrm{m}}{\partial y}+\alpha(T-T_0)g\cos\Omega_\mathrm{d}\tau+\nu\nabla^2 v-2\Omega_\mathrm{d}u-\Omega_\mathrm{d}^2\alpha(T-T_0)y \tag{3}$$

where

$$\frac{\partial p_\mathrm{m}}{\partial x}=-\frac{\partial p}{\partial x}+\rho_0\Omega_\mathrm{d}^2 x-\rho_0 g\sin\Omega_\mathrm{d}\tau$$
$$\frac{\partial p_\mathrm{m}}{\partial y}=-\frac{\partial p}{\partial y}+\rho_0\Omega_\mathrm{d}^2 y-\rho_0 g\cos\Omega_\mathrm{d}\tau \tag{4}$$
$$\frac{\mathrm{D}T}{\mathrm{D}\tau}=\kappa\nabla^2 T$$

No-slip boundary conditions are imposed for the velocity components at all the walls. T is assumed to satisfy thermally conducting boundary conditions at the vertical side walls, while Neumann boundary conditions $\frac{\partial T}{\partial y}=0$ are assumed for the horizontal top and bottom walls as shown in Fig. 1.

On performing non-dimensionalization using reference length, velocity, time and pressure scales as H, $\frac{\kappa}{H}$,

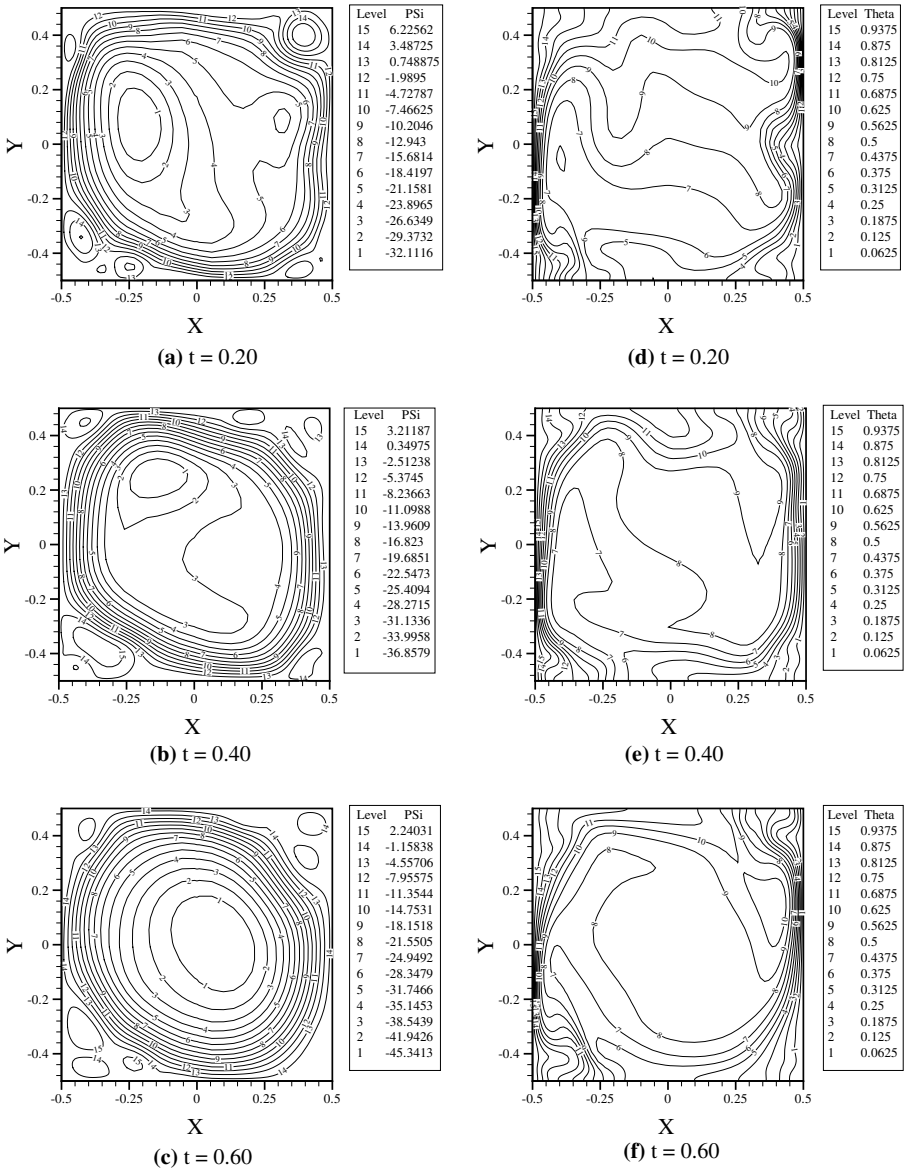

Fig. 5. (a), (b) and (c) show streamline contours while (d), (e) and (f) show isotherm contours for different time instants for $Ra=10^7$, $Ta=8.16\times10^4$ and $Ra_\mathrm{w}=1.02\times10^6$.

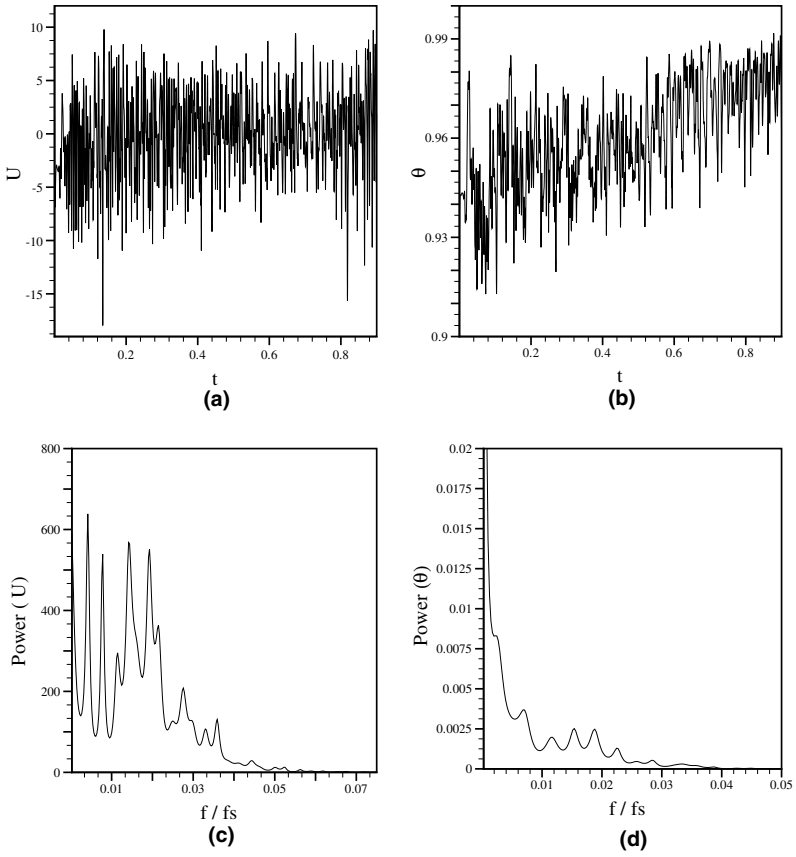

Fig. 6. (a) and (b) show time history while (c) and (d) shows power spectrum of horizontal velocity component (U) and temperature (θ) at spatial point (a) for $Ra = 10^7$, $Ta = 8.16 \times 10^4$ and $Ra_w = 1.02 \times 10^6$.

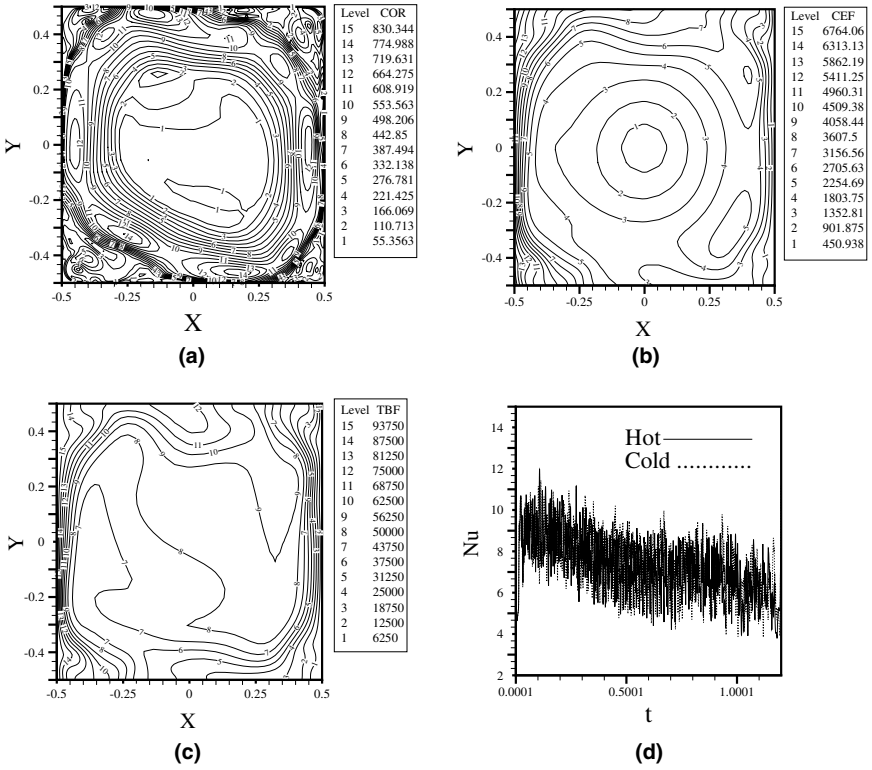

Fig. 7. Depicts spatial variation of (a) Coriolis force, (b) centrifugal force, (c) thermal buoyancy force at $t = 0.4$ and (d) variation of Nusselt number Nu with time for $Ra = 10^7$, $Ta = 8.16 \times 10^4$ and $Ra_w = 1.02 \times 10^6$.

$\frac{H^2}{\kappa}$, and $\frac{\rho\kappa^2}{H^2}$ respectively, the governing equations, initial and boundary conditions, become

$$\frac{\partial U}{\partial X}+\frac{\partial V}{\partial Y}=0 \tag{5}$$

$$\frac{\mathrm{D}U}{\mathrm{D}t}=-\frac{\partial P_{\mathrm{m}}}{\partial X}+Pr\nabla^2 U+RaPr\theta\sin(\Omega t)+Ta^{0.5}PrV - Ra_{\mathrm{w}}PrX\theta \tag{6}$$

$$\frac{\mathrm{D}V}{\mathrm{D}t}=-\frac{\partial P_{\mathrm{m}}}{\partial Y}+Pr\nabla^2 V+RaPr\theta\cos(\Omega t)-Ta^{0.5}PrU - Ra_{\mathrm{w}}PrY\theta \tag{7}$$

$$\frac{\mathrm{D}\theta}{\mathrm{D}t}=\nabla^2\theta \tag{8}$$

In Eq. (8) we have neglected viscous dissipation and pressure work due to incompressibility of the flow.

The initial conditions are

At $t<0 \quad U=V=0 \quad$ and $\quad \theta=0.5 \quad$ for all X and Y

While the boundary conditions become

At $t \geqslant 0$

$$X=0,1; \quad Y=0; \quad U=V=0; \quad \frac{\partial\theta}{\partial Y}=0$$

$$X=0,1; \quad Y=1; \quad U=V=0; \quad \frac{\partial\theta}{\partial Y}=0$$

$$Y=0,1; \quad X=0; \quad U=V=0; \quad \theta=1$$

$$Y=0,1; \quad X=1; \quad U=V=0; \quad \theta=0$$

The space-averaged Nusselt number at both the cold and hot walls has been calculated using the relation

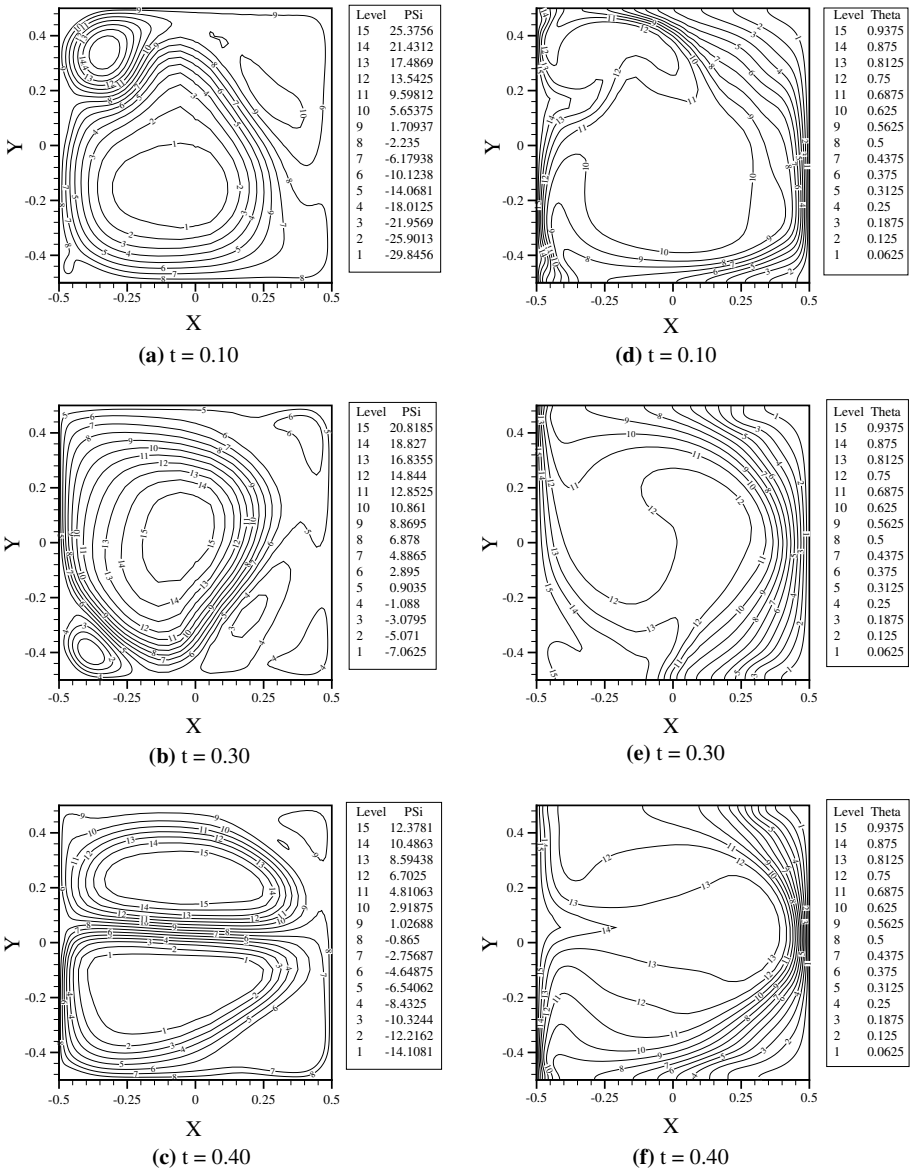

(a) t = 0.10 **(d)** t = 0.10

(b) t = 0.30 **(e)** t = 0.30

(c) t = 0.40 **(f)** t = 0.40

Fig. 8. (a), (b) and (c) show streamline contours while (d), (e) and (f) show isotherm contours at different time instants for $Ra=10^7$, $Ta=8.16\times10^6$ and $Ra_{\mathrm{w}}=1.02\times10^8$.

$$\overline{Nu} = -\frac{1}{H}\int_0^1 \frac{\partial\theta}{\partial X}\,\mathrm{d}Y \tag{9}$$

The numerical scheme used to solve the equations has been explained in detail in Hasan and Baig [15]. In this scheme, the non-linear convective terms in Eqs. (6)–(8) have been evaluated using third-order accurate upwind scheme in the interior with first-order upwind scheme near the walls. The viscous diffusion terms are discretized using the three-point central differencing stencil, while time integration has been performed explicitly using Adam-Bashforth second-order accurate scheme in order to capture the unsteady physics associated with the oscillatory flow regime. A non-uniform collocated mesh of 71×71 grid point has been generated, with the minimum spacing of 0.002 near the walls and maximum spacing of 0.046 near the center of the cavity. The mass continuity has been enforced by solving Poisson equation for pressure, using Strongly Implicit Procedure (SIP), as implemented in [17] with a significantly small L_2-norm tolerance limit of 10^{-9}.

Regarding grid-independence, we simulated the flow on a grid of 91×91 keeping the location of first grid point constant and found that the integral parameters such as mean Nu number changed by less than 3% while qualitative change in spatial patterns remains is insignificant. Hence in order to cut down the computational time, we ran all our simulation cases on a coarser grid of 71×71. We have considered three spatial points (a), (b) and (c) having coordinate locations $(X, Y) = (-0.4933, -0.4933)$, $(-0.2816, -0.2816)$ and $(0.372, 0.372)$ on which temporal history of several dynamical variables has been recorded.

2.1. Validation

The numerical code developed has been validated by solving the glazing problem i.e. buoyancy driven flow

Table 1
Validation of code with numerical results of Nonino and Croce [16]

Ra	$\lvert\Psi_{\max}\rvert$	$\lvert U_{\max}\rvert$	$\lvert V_{\max}\rvert$	Nu_{avg}	Reference
10^5	9.652	35.668	68.367	4.483	Present
10^5	9.618	34.749	68.646	4.521	Benchmark [16]
10^6	16.948	65.589	221.488	8.749	Present
10^6	16.817	64.827	220.630	8.825	Benchmark [16]
10^7	30.638	145.460	697.669	16.284	Present
10^7	30.165	148.590	699.670	16.522	Benchmark [16]

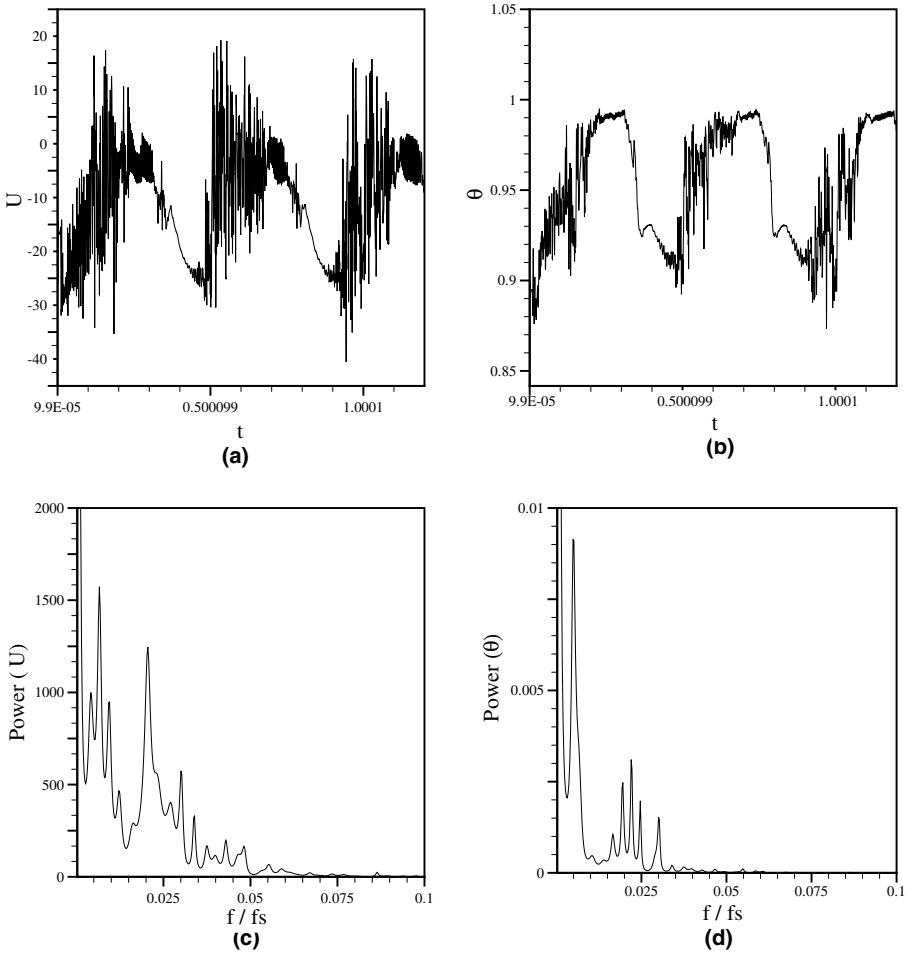

Fig. 9. (a) and (b) show time history while (c) and (d) show power spectrum of horizontal velocity component (U) and temperature (θ) at spatial point (a) for $Ra = 10^7$, $Ta = 8.16 \times 10^6$ and $Ra_w = 1.02 \times 10^8$.

inside a square cavity with differentially heated vertical walls and horizontal adiabatic walls. The results have been compared with the benchmark solutions of Nonino and Croce [16]. The range of Ra considered is between 10^5 and 10^7 while Pr is taken to be 0.71. Table 1 shows the comparison between the results of present study and benchmark solution. The minimum and maximum grid spacing employed was 0.004 and 0.048 respectively, with total number of grid points being equal to 55, in both spatial directions as in the benchmark study. The maximum percentage error in $|\Psi_{\max}|$, $|U_{\max}|$, $|V_{\max}|$ and Nu_{avg} are respectively equal to 1.568%, 2.106%, 0.406% and 1.440% respectively.

3. Results and discussion

3.1. Effects of increasing centrifugal and Coriolis forces

In order to analyse the effects of increasing centrifugal and Coriolis forces, we have performed several runs of the code with increasing rotational speed Ω, keeping the $Ra = 10^7$ as constant.

For $Ra = 10^7$ at low rotational speeds ($Ta = 8.16$ and $Ra_w = 1.02 \times 10^2$), corresponding to non-dimensional rotation $\Omega = 0.014$, the thermal buoyancy is the dominating force and this is also evident from Fig. 2 which shows multi-cellular roll pattern of stream function. The isotherms show thin boundary layers near isothermal walls with stable stratification of the core. The dynamical variables U and θ in Fig. 3 exhibit a chaotic time-signal at both the co-ordinate points (a) and (b). The corresponding power spectrum too exhibits a broad range of frequencies at both coordinate points (a) and (b). These features characterize a strong turbulent flow in the cavity. The spatial distribution of forces in Fig. 4 shows thermal buoyancy is the dominating force compared to smaller magnitudes of Coriolis and centrifugal forces. From Fig. 4(d), it is clear that spatially averaged $\overline{Nu}$ shows oscillatory heat transfer at both the walls with a temporal mean value of 8.5 approximately.

As the rotational speed is increased corresponding to non-dimensional $\Omega = 1.428$ ($Ta = 8.16 \times 10^4$ and $Ra_w = 1.02 \times 10^6$), the stream functions in Fig. 5 again show formation of multiple rolls of slightly larger magnitude compared to the previous case. The isotherms depict

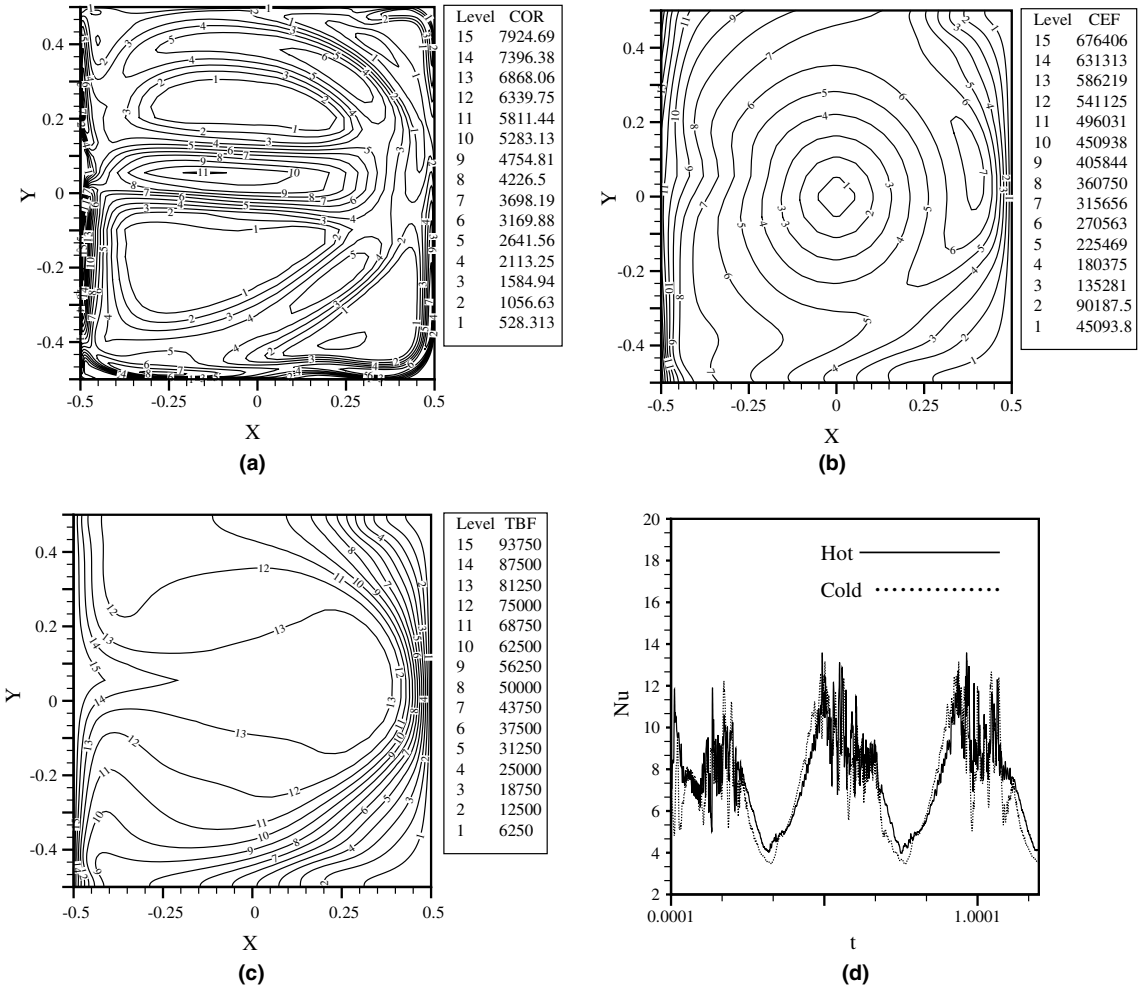

Fig. 10. Shows spatial variation of (a) Coriolis force, (b) centrifugal force, (c) thermal buoyancy force at $t = 0.4$ and (d) variation of Nusselt number Nu with time for $Ra = 10^7$, $Ta = 8.16 \times 10^6$ and $Ra_w = 1.02 \times 10^8$.

beginning of unstable stratification in the core signifying increase in convective motion in the core of the cavity. The dynamical variables U and θ in Fig. 6 exhibit chaotic time-signal trace at all and the power spectra reinforce that view. The spatial variation of forces show (Fig. 7) stronger Coriolis and centrifugal forces near the walls but still their magnitude is quite small compared to thermal buoyancy force. From Fig. 7(d), it is clear that $\overline{Nu}$ shows oscillatory heat transfer at the walls with the mean value around 5.0. Hence the heat transfer at both the walls is appreciably reduced due to 100-fold increase in Ω as compared to the previous case.

Further 10-fold increase of rotation corresponding to $\Omega = 14.285$ ($Ta = 8.16 \times 10^6$ and $Ra_w = 1.02 \times 10^8$), results in drastic change in pattern formation of stream functions rolls as is evident in Fig. 8(a)–(c). These figures show formation of counter-rotating rolls which occupy whole of the enclosure. These rolls are primarily formed due to the action of centrifugal force on the fluid. Isotherms in Fig. 8(d)–(f) show generation of mushroom-shaped structure in the core of the cavity which leads to strong unstable stratification of the core. The time history in Fig. 9 depicts a stronger turbulent time-signal at all the co-ordinate points while the corresponding power spectra show an increase of two to three times more power than the previous case. Fig. 10(a)–(c) shows that in the core of the cavity centrifugal and Coriolis forces are more dominant especially there is large magnitude of centrifugal force from centre of hot wall towards the cold wall which leads to formation of mushroom-shaped isotherms. Fig. 10(d) shows unsteady almost cyclic heat transfer at the walls. The minima correspond to the time interval when thermal buoyancy is dominant while the maxima correspond to the duration when centrifugal force is the dominating force.

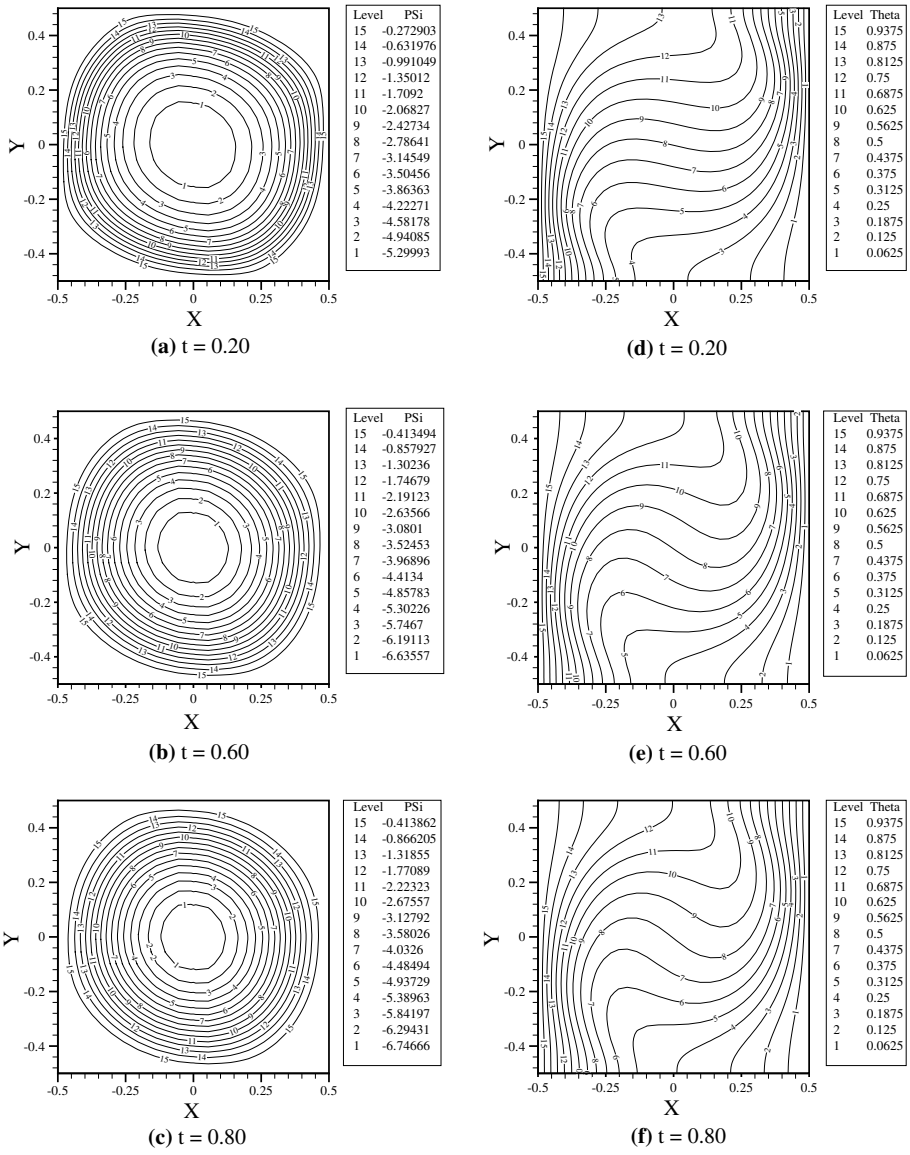

Fig. 11. (a), (b) and (c) show streamline contours while (d), (e) and (f) show isotherm contours for different time instants for $Ra = 10^5$, $Ta = 8.16 \times 10^4$ and $Ra_w = 1.02 \times 10^4$.

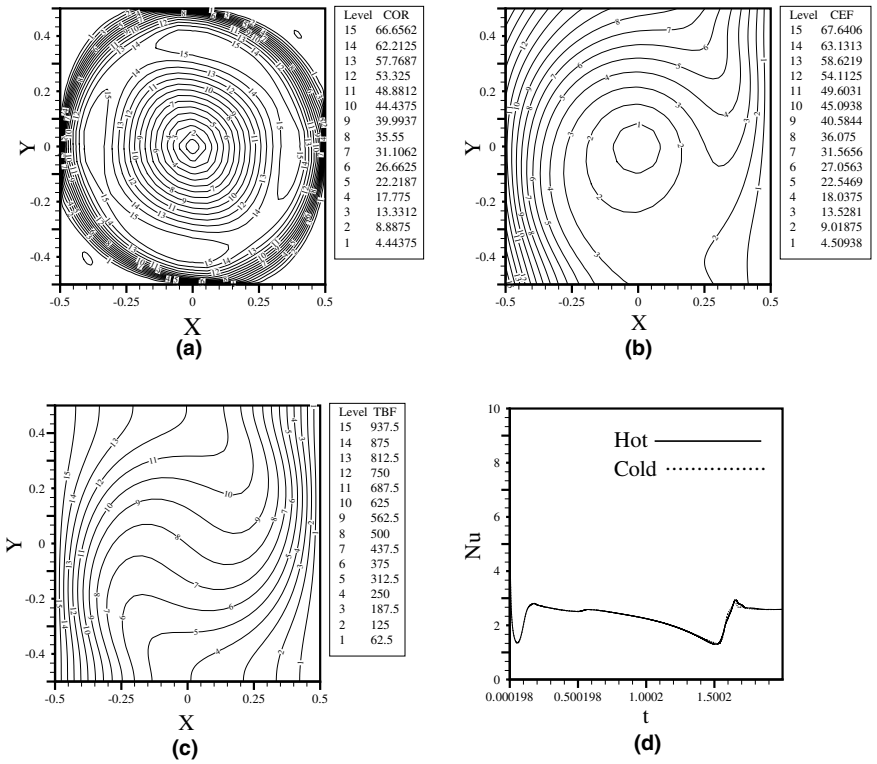

Fig. 12. Depicts spatial distribution of (a) Coriolis force, (b) centrifugal force, (c) thermal buoyancy force at $t = 0.4$ and (d) variation of Nusselt number Nu with time for $Ra = 10^5$, $Ta = 8.16 \times 10^4$ and $Ra_w = 1.02 \times 10^4$.

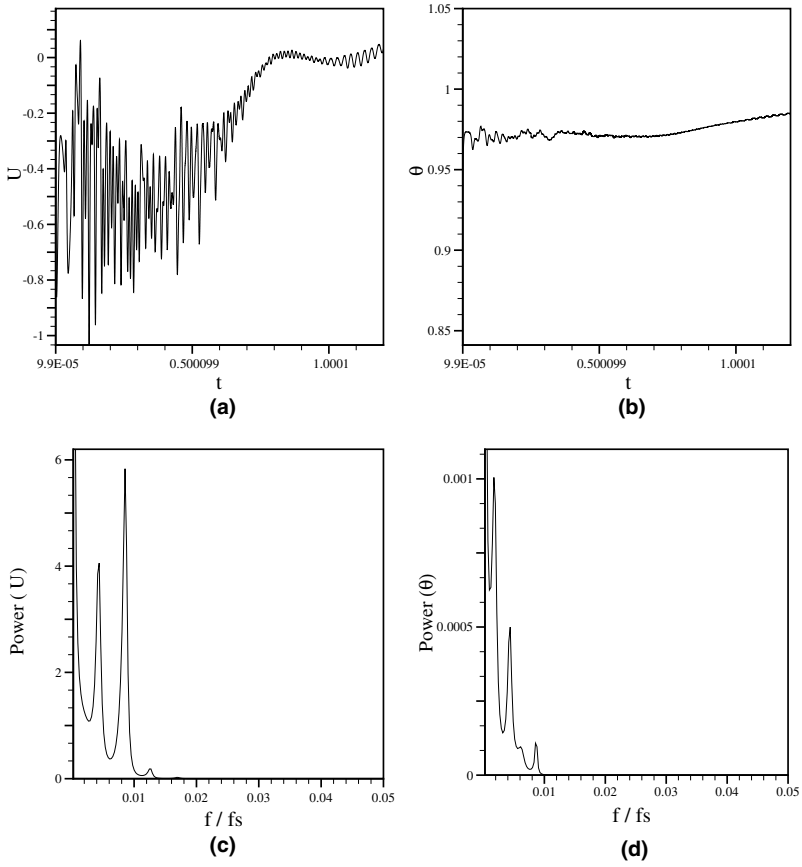

Fig. 13. (a) and (b) show time history while (c) and (d) show power spectrum of horizontal velocity component (U) and temperature (θ) at spatial point (a) for $Ra = 10^6$, $Ta = 8.16 \times 10^4$ and $Ra_w = 1.02 \times 10^5$.

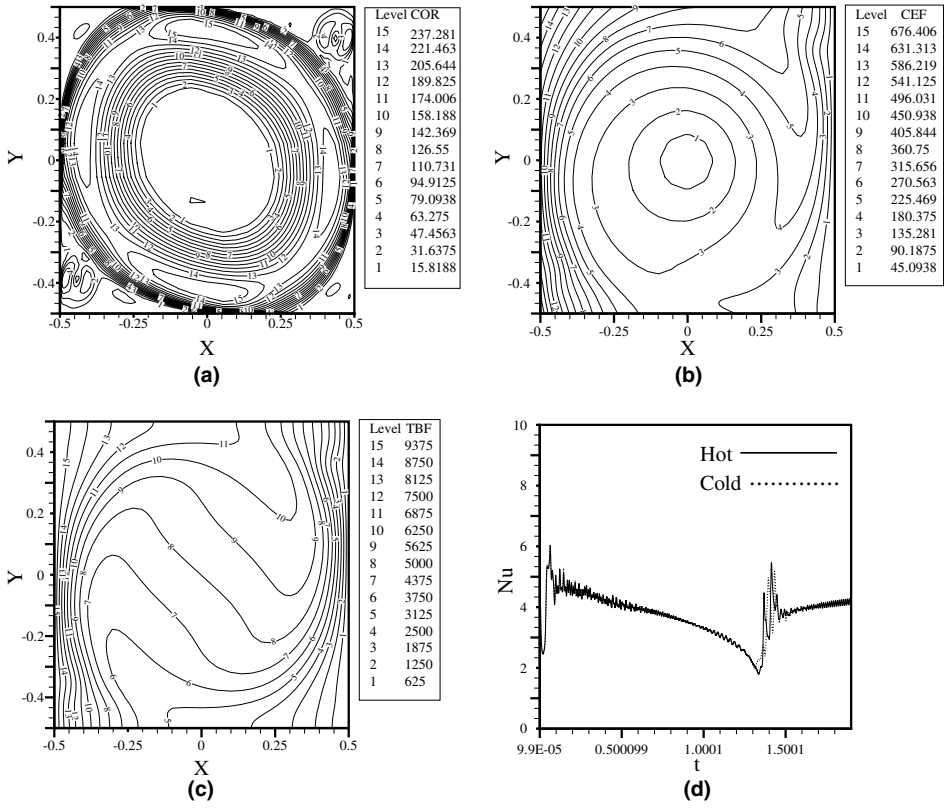

Fig. 14. Shows spatial distribution of (a) Coriolis force (b) centrifugal force (c) thermal buoyancy force at $t = 0.4$ and (d) variation of Nusselt number Nu with time for $Ra = 10^6$, $Ta = 8.16 \times 10^4$ and $Ra_w = 1.02 \times 10^5$.

3.2. Effects of increasing thermal buoyancy force

These simulations have been performed keeping the non-dimensional rotational speed $\Omega = 1.428$ ($Ta = 8.16 \times 10^4$ and $Ra_w = 1.02 \times 10^4$) constant while the Ra is varied from 10^5 to 10^7. For the case when $Ra = 10^5$, the stream functions exhibit a single clockwise roll almost occupying the whole cavity as shown in Fig. 11. The corresponding isotherms depict thick boundary layers near the isothermal walls with stable stratification in the core of the enclosure. The time history depicts steady flow at all the co-ordinate points with the power density spectrums further corroborating that view. The spatial variation of forces in Fig. 12(a)–(c) show thermal buoyancy as the main dominating force. From Fig. 12(d) it is clear that $\overline{Nu}$ shows steady heat transfer at the walls with a value of 2.8.

Further increase of Ra to 10^6 for same Ω as in the previous case, results in stream function rolls becoming more stronger but the the overall pattern remains the same. The isotherms show a comparably thinner thermal boundary layer near the walls and also there is onset of convective motion in the core of the cavity. The time history of velocity component U as well as temperature θ in Fig. 13 depicts a quasi-periodic time signal at all the spatial points. The power spectra show quasi-periodicity with a fundamental frequency and two to three sub-harmonics at all the coordinate points. Fig. 14 shows the spatial variation of forces which still exhibits the domination of thermal buoyancy force with the centrifugal force getting stronger in the core of the cavity. From Fig. 14(d) it is clear that $\overline{Nu}$ shows oscillatory heat transfer at the walls with a mean value of 4.0 approximately.

3.3. Heat transfer analysis

The plots (a) and (b) in Fig. 15 shows the effect on heat transfer at fixed $Ra = 10^7$ as rotational speed Ω is increased slightly from 0 to 0.014. From these plots it is apparent that there is no effect on magnitude of $\overline{Nu}$. Fig. 15(c) shows that at $\Omega = 1.428$, the magnitude of $\overline{Nu}$ has appreciably decreased to a mean value of around 7.0. Further increase of Ω to 14.285 results in significant change in $\overline{Nu}$ variation with time. The possible source of almost cyclic rise and fall of $\overline{Nu}$ is due to alternate domination of thermal buoyancy and centrifugal forces. As Ω is increased further to a large value of 71.428, the $\overline{Nu}$ shows an appreciable rise to a mean value around 16.0.

These change can be explained that at lower to medium rotational speeds there is disruption of heat transfer by opposing interaction of thermal and rotational buoyancy which results in decrease of $\overline{Nu}$. For rotational speeds larger than a critical speed, the heat transfer is governed by

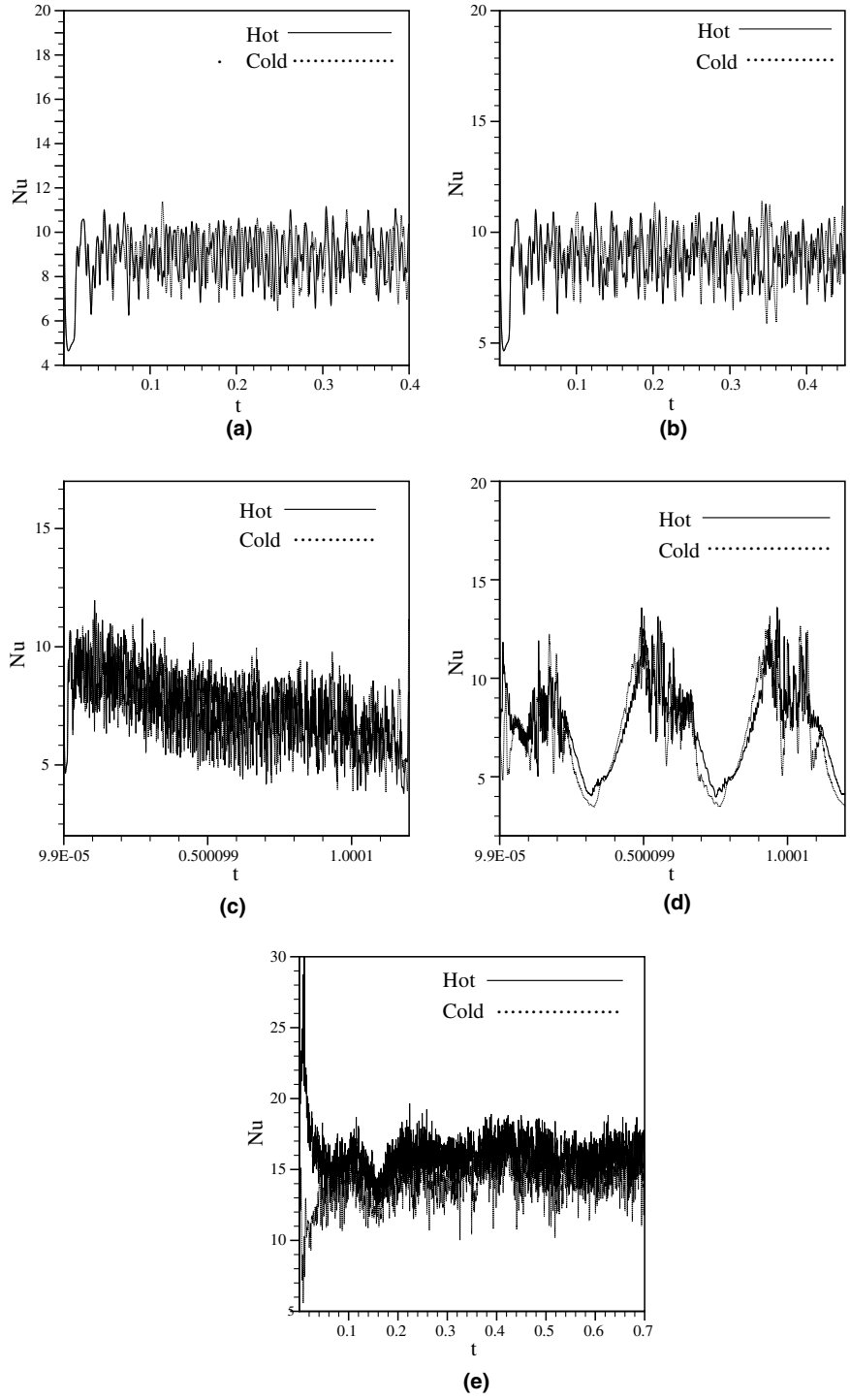

Fig. 15. Variation of Nu for different Ta and Ra_w at $Ra = 10^7$: (a) $Ta = 0$, $Ra_w = 0$; (b) $Ta = 8.16$, $Ra_w = 1.02 \times 10^2$; (c) $Ta = 8.16 \times 10^4$, $Ra_w = 1.02 \times 10^6$; (d) $Ta = 8.16 \times 10^6$, $Ra_w = 1.02 \times 10^8$; and (e) $Ta = 2.04 \times 10^8$, $Ra_w = 2.55 \times 10^9$.

centrifugal forces and occurs not through the boundary layers but by the mushroom-shaped structure and hence there is rise of $\overline{Nu}$.

4. Conclusions

The following conclusions can be derived on basis of the numerical experiments:

1. Increase in the thermal buoyancy force with increasing Ra generates thinner boundary layers which in turn increases heat transfer at the isothermal walls of the cavity.
2. Primary roll pattern changes into a multi-cellular roll pattern as Ra is increased keeping Ω constant.
3. At higher value of Ω i.e. at larger values of Ta and Ra_w, two horizontally aligned counter-rotating rolls are obtained. This leads to generation of mushroom-shaped

structure isotherms in the core of the cavity with unstable thermal stratification.

4. This significantly higher strength of counter-rotating rolls generated by the centrifugal force in the core of the cavity lead to enhanced heat transfer.
5. At the rotational speed $\Omega = 14.285$ there is alternate domination of centrifugal and thermal buoyancy forces and this results in almost periodic variation of Nusselt number with time.
6. At very high rotational speeds corresponding to the case $\Omega = 71.428$, there is a significant increase in Nusselt number which is primarily due to domination of centrifugal force.

References

[1] W. Nakayama, Forced convective heat transfer in a straight pipe rotating around a parallel axis (2nd report, Turbulent region), Int. J. Heat Mass Transfer 11 (1968) 1185–1201.

[2] Y. Mori, W. Nakayama, Forced convection heat transfer in straight pipe rotating around a parallel axis (1st report, Laminar region), Int. J. Heat Mass Transfer 10 (1967) 1179–1194.

[3] B. Weigand, H. Beer, Fluid flow and heat transfer in a rotating pipe subjected to external convection, Int. J. Heat Mass Transfer 35 (1992) 1803–1809.

[4] A.R. Johnson, W.D. Morris, An experimental investigation into the effects of rotation on the isothermal flow resistance in circular tubes rotating about a parallel axis, Int. J. Heat Mass Transfer 13 (1992) 132–140.

[5] C.T. Nguyen, H. Bazzi, J. Orfi, Numerical investigation of the effects of rotation on a germanium float zone under micro-gravity conditions, Numer. Heat transfer, Part A 28 (1995) 2667–2685.

[6] M. Mahadevappa, K.V.C. Rao, V.M.K. Sastri, Numerical study of fully developed fluid flow and heat transfer in rectangular and elliptical ducts rotating about a parallel axis, Int. J. Heat Mass Transfer 39 (1996) 867–875.

[7] K.T. Lee, H.L. Tsai, W.M. Yan, Mixed convection heat and mass transfer in vertical rectangular ducts, Int. J. Heat Mass Transfer 40 (1997) 1621–1631.

[8] G.J. Hwang, T.C. Jen, Convective heat transfer in rotating isothermal ducts, Int. J. Heat Mass Transfer 33 (1990) 1817–1828.

[9] S. Fann, W.J. Yang, Hydrodynamically and thermally developing laminar flow through rotating channels having isothermal walls, Numer. Heat Mass transfer, Part A 22 (1992) 257–288.

[10] Y. Mori, T. Fudaka, W. Nakayama, Convective heat transfer in rotating circular pipe (2nd report), Int. J. Heat Mass Transfer 14 (1971) 1807–1824.

[11] W.-M. Yan, Mixed convection heat and mass transfer in rectangular ducts rotating about parallel axis, Int. J. Heat Mass Transfer 42 (1999) 2955–2965.

[12] F. Song, D. Ewing, C.Y. Ching, Fluid flow and heat transfer model for high speed rotating heat pipes, Int. J. Heat Mass Transfer 46 (2003) 4393–4401.

[13] T. Yang, L. Wang, Bifurcation and stability of combined free and convection in rotating curved ducts of square cross-section, Int. J. Heat Mass Transfer 46 (2003) 613–629.

[14] Y.T. Ker, T.F. Lin, A combined numerical and experimental study of air convection in a differentially heated cubic cavity, Int. J. Heat Mass Transfer 39 (1996) 3193–3210.

[15] N. Hasan, M.F. Baig, Evolution to aperiodic penetrative convection in odd shaped rectangular enclosures, Int. J. Numer. Methods Heat Fluid Flow 12 (8) (2002) 895–915.

[16] C. Nonino, G. Croce, An equal-order velocity–pressure algorithm for incompressible thermal flows, Numer. Heat Transfer, Part B 32 (1997) 17–35.

[17] J.H. Ferziger, M. Peric, Computational Methods for Fluid Dynamics, third ed., Springer-Verlag, 2003, pp. 101–105.